## Title

Tunable Picoliter-Scale Dropicle Formation Using Amphiphilic Microparticles with Patterned Hydrophilic Patches.



## Journal

Advanced Science, 12(12)

## Authors

Song, Xinpei
Udani, Shreya
Ouyang, Mengxing
et al.

## Publication Date

2025-03-01

## DOI

10.1002/advs.202411014

Peer reviewed

ADVANCED SCIENCE Open Access
www.advancedscience.com

# Tunable Picoliter-Scale Dropicle Formation Using Amphiphilic Microparticles with Patterned Hydrophilic Patches

*Xinpei Song, Shreya Udani, Mengxing Ouyang, Mehmet Akif Sahin, Dino Di Carlo,* and Ghulam Destgeer**

**Microparticle-templated droplets or *dropicles* have recently gained interest in the fields of diagnostic immunoassays, single-cell analysis, and digital molecular biology. Amphiphilic particles have been shown to spontaneously capture aqueous droplets within their cavities upon mixing with an immiscible oil phase, where each particle templates a single droplet. Here, an amphiphilic microparticle with four discrete hydrophilic patches embedded at the inner corners of a square-shaped hydrophobic outer ring of the particle (4C particle) is fabricated. Three dimensional computational fluid dynamics simulations predict droplet formation dynamics and differing equilibrium conditions depending on the patterning configuration. Experiments recapitulate equilibrium conditions, enabling tunable dropicle configurations with reproducible volumes down to ≈200 pL templated by the amphiphilic particles. The dropicle configurations depend predominantly on the size of the hydrophilic patches of the 4C particles. This validates that the modeling approach can inform the design of dropicles with varying volumes and numbers per particle, which can be harnessed in new amplified bioassays for greater sensitivity, dynamic range, and statistical confidence.**

## 1. Introduction

Microparticle-templated droplets or *dropicles* result from either spontaneous or shear-induced partitioning of an aqueous volume within an immiscible continuous oil phase.[1–8] Dropicles have recently gained interest in the fields of diagnostic immunoassays,[9–13] single-cell analysis,[14–17] and digital molecular biology[18] for their ability to democratize and scale up microfluidic droplet assays that typically require complex instrumentation.[19–23] Amphiphilic microparticles, with outer hydrophobic and inner hydrophilic polymer layers, allow for spontaneous droplet formation as the aqueous phase stays within the hydrophilic cavity, reaching a stable lower energy state.[1–5] These previously reported amphiphilic microparticles,[1–5] fabricated using a stop-flow lithography process,[24–30] had an inner *continuous* hydrophilic layer that templated a single droplet within the particle cavity. The particle fabrication parameters were manipulated to allow for varying particle morphologies and encapsulate a broad range of droplet volumes (0.25 to 30 nL).[3,5] These dropicles with volumes *O*(nL) were used to detect analytes with a detection limit of 10 pg mL$^{-1}$ in buffer[2] and 50 pg mL$^{-1}$ in serum.[4] For enhanced bioassay sensitivity and accuracy, it is essential to reduce the volume of segmented droplets and increase the number of individual compartments per assay for better statistical confidence. One way to achieve this is to fabricate smaller amphiphilic particles with even tinier cavities to hold droplets with volumes *O*(pL). However, such an approach is plagued with challenges on the fabrication end, such as difficulty stopping the flow in smaller microfluidic channels, as depicted in our earlier work.[3] Therefore, an out-of-the-box approach is required to fabricate new particle designs that can hold smaller droplet volumes *O*(pL) without significantly reducing the particle size.

The dropicle formation depends on the amphiphilic particle's shape and polymer distribution, which is defined by a 3D-printed microfluidic device that could sculpt multiple co-flowing streams in a target cross-sectional shape.[2–4] However, it is costly and time-consuming to experimentally vary the design of the microfluidic devices for modulating the characteristics of the

X. Song, M. A. Sahin, G. Destgeer
Control and Manipulation of Microscale Living Objects
Center for Translational Cancer Research (TranslaTUM)
Munich Institute of Biomedical Engineering (MIBE)
Department of Electrical Engineering
School of Computation, Information and Technology (CIT)
Technical University of Munich
Einsteinstraße 25, 81675 Munich, Germany
E-mail: ghulam.destgeer@tum.de
S. Udani, M. Ouyang, D. Di Carlo
Department of Bioengineering
University of California Los Angeles
Los Angeles, CA 90095, USA
E-mail: dicarlo@ucla.edu

The ORCID identification number(s) for the author(s) of this article can be found under https://doi.org/10.1002/advs.202411014



**DOI: 10.1002/advs.202411014**

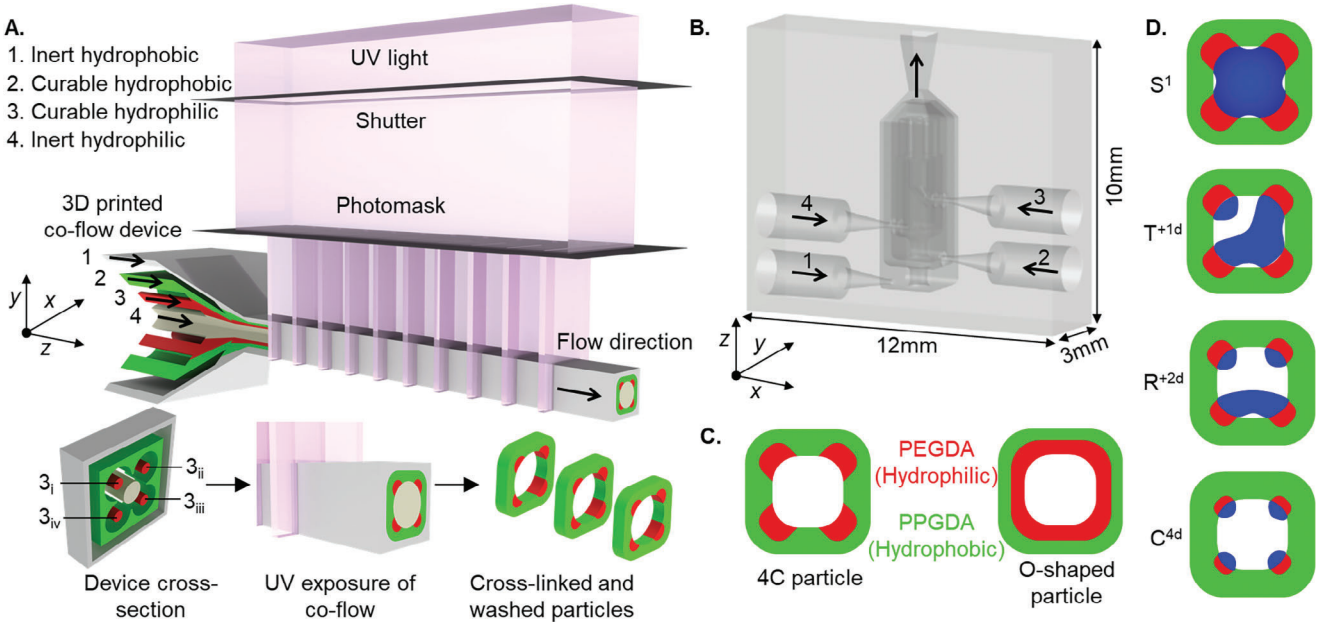


**Figure 1.** A) Schematic of the 3D printed microfluidic device for 4C particle fabrication using the stop-flow lithography process. B) A to-the-scale model of the 3D microfluidic device. C) Comparison between the 4C and O-shaped particles composed of hydrophilic polyethylene glycol diacrylate (PEGDA) and hydrophobic polypropylene glycol diacrylate (PPGDA). D) Four different dropicle configurations are driven by the tunable design of 4C particles.

fabricated particle. Therefore, the first step toward the desired dropicle formation by optimizing the particle parameters is to meticulously design the microfluidic devices using numerical models. Numerical simulations offered an indispensable way to predict the particle's characteristics before the 3D printing of the microfluidic device and fabricating the particles. We have previously used single-phase flow simulations to predict the shape of the sculpted flow profile inside microfluidic channels.[2] However, these numerical models do not account for the variable viscosities of different co-flowing streams. Therefore, a two-phase flow model is required to simulate variable viscosity co-flowing streams and obtain an accurate sculpted flow cross-section before particle fabrication.

Moreover, numerical modeling of dropicle formation before experimental testing of new particle designs could save precious lab resources and time. To this end, mathematical models minimizing the interfacial energy are introduced to simulate uniform droplet volumes templated by single-material crescent or multi-material cylindrical particles.[31,32] Recently, we have established and analyzed a 2D computational fluid dynamic (CFD) model to simulate the interface of immiscible water and oil phases for dropicle formation within concentric amphiphilic particles.[33] The numerical findings matched well with the experimental results.[3] A 2D CFD model can be suitable for symmetric particle geometries, e.g. O-shaped particles, with a reasonable computational cost. However, it cannot encompass complex particle shapes with anisotropic material distribution and asymmetric dropicle formation. Therefore, a 3D CFD model is required to understand the formation of dropicles in various shapes dictated by the shape of the amphiphilic particle.

In this work, we demonstrate amphiphilic particle designs with four discrete and carefully patterned hydrophilic regions embedded within the four corners of a square-shaped hydrophobic backbone (4C particles). We study, computationally and experimentally, the ability of 4C particles to form picoliter-scale localized droplets. We designed and 3D printed a multi-channel microfluidic device to sculpt a multi-layered laminar flow of polymer precursors and fabricate the 4C particles using a "stop flow lithography" process (**Figure** 1A,B). We performed two-phase flow simulations to predict the shape of the particles by the sculpted flow profile, defined by variable viscosity polymer precursor streams, within the outlet channel of the device. The fabricated 4C particles with tunable physio-chemical characteristics were later used to template one to four droplets per particle of varying volumes *O*(pL) and morphologies, such that a single square droplet ($S^1$), a triangular droplet accompanied by one small droplet ($T^{+1d}$), a rectangular droplet accompanied by two small droplets ($R^{+2d}$) or four individual droplets at the corners ($C^{4d}$) were captured by the 4C particles (Figure 1C,D). We also developed a 3D numerical model to describe the formation of variable dropicle configurations and study how the dropicle shape can evolve over time due to particle characteristics, swelling, and trapped aqueous volume. By enabling droplet configurations with varying numbers of droplets and volumes per droplet, our platform supports multiplexed assays with tunable dynamic ranges. For some biomolecule targets that require higher sensitivity, larger reaction volumes (such as those generated by single-droplet particles) are optimal.[2,4] This ensures sufficient signal detection at low analyte concentrations. In contrast, for targets with narrower or higher dynamic ranges, using particles that template multiple smaller droplets can provide better statistical accuracy and efficiency. This flexibility enhances the versatility of our platform in bioanalytical applications and offers significant advantages for clinical workflows, such as reducing sample size and minimizing costs.

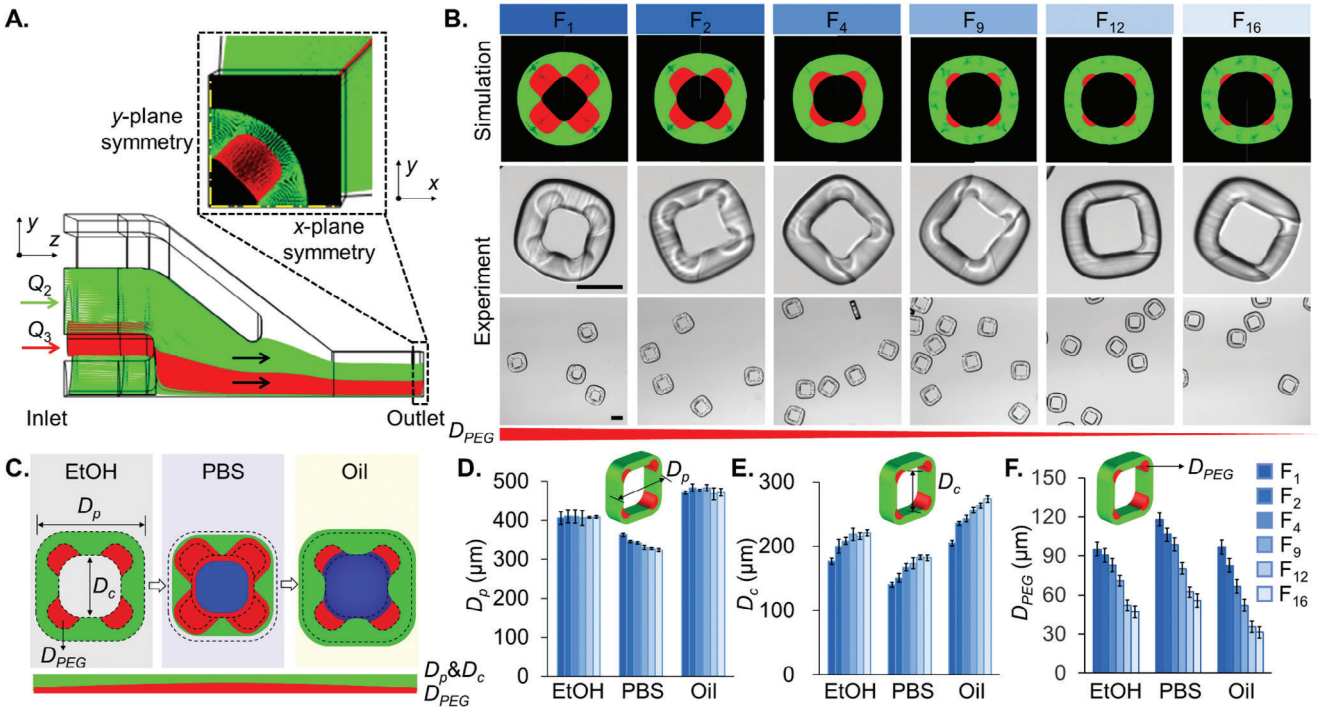


**Figure 2.** Particle fabrication and characterization. A) Quarter 3D model of the microfluidic device to generate the particle. B) Simulated and experimental particles with different flow rate ratios. The top row shows the simulated particles in the form of velocity streamlines at the outlet of the microchannels. The following two rows are the experimentally observed particles, with a zoomed view of a single particle (middle) and multiple particles (bottom) in EtOH. Scale bar: 200 μm. C) The geometrical morphology of the 4C amphiphilic microparticles as the solution is exchanged from EtOH to PBS to oil. D–F) Distributions of $D_p$, $D_c$, and $D_{PEG}$ in EtOH, PBS, and oil with different flow rate ratios. The inserts are the schematics of the particles with corresponding dimensions being characterized.

## 2. Results and Discussion

### 2.1. 4C Particle Fabrication and Characterization

We performed a 3D numerical simulation of fluid flow through the microfluidic device (quarter domain) to predict the cross-sectional profile of the sculpted flow (**Figure 2A**). The green and red color streamlines indicate the curable hydrophobic and hydrophilic precursor streams, respectively, that will define the particle shape. The flow rate ratios of the four streams $Q_{1,2,4}$:$Q_3$ were varied as 1:1, 2:1, 4:1, 9:1, 12:1, and 16:1, to obtain $F_1$, $F_2$, $F_4$, $F_9$, $F_{12}$, and $F_{16}$ particles, respectively. The flow rate ratio was increased while maintaining a constant total flow rate ($Q_T = Q_1 + Q_2 + Q_3 + Q_4$) to gradually decrease the hydrophilic patch size of the 4C particles from $F_1$ to $F_{16}$ (Figure 2B). The particle shape predicted by the CFD simulation matched with the cured particles suspended in ethanol (EtOH); however, minor discrepancies between the experimental and numerical results could be attributed to the fact that the cured particles deformed slightly after they were transferred from a polymer precursor solution to pure EtOH solution (see also Figure S1, Supporting Information).

The medium around particles is sequentially changed from EtOH to phosphate-buffered saline (PBS) to oil for dropicle formation (Section 2.2). The particle ($D_p$), cavity ($D_c$), and hydrophilic patch ($D_{PEG}$) diameters measured in EtOH, PBS, and oil showed reasonable uniformity within each particle type (Figure 2C–F). The hydrophilic patches swelled after absorbing the aqueous PBS solution, whereas the outer hydrophobic layer contracted as the solution was exchanged from EtOH to PBS. Subsequently, the hydrophobic layer absorbed oil to swell in the solution exchange from PBS to oil, increasing the particle and cavity diameters, whereas the hydrophilic patch size reduced close to their original size in EtOH (Figure 2C). In EtOH, all the particle types ($F_1$ to $F_{16}$) showed a narrow size distribution with $D_p$ of 409 ± 3 μm, even though we used very different flow rate ratios during the fabrication process, which highlights the consistency of the backbone structure of the particles (Figure 2D). However, upon medium exchange from EtOH to PBS, each particle type contracted differently following the hydrophobic to hydrophilic polymer ratio within a particle. The $F_1$ particle, with the lowest proportion of hydrophobic polymer, shrank the least from $D_p \approx 406$ μm to ≈363 μm (≈11%), whereas $F_{16}$ particles, with the highest proportion of hydrophobic polymer, shrank the most from $D_p \approx 409$ μm to ≈324 μm (≈21%). As the medium was exchanged from PBS to oil, all the particle types ($F_1$ to $F_{16}$) expanded beyond their original sizes in EtOH, with an average $D_p \approx 475 \pm 7$ μm. For example, the $F_1$ and $F_{16}$ particles expanded back by ≈30% and ≈46% from PBS to oil, respectively. A higher expansion of $F_{16}$ particles can be attributed to the soaking of a relatively thicker hydrophobic layer by oil. A variable expansion of $F_1$-$F_{16}$ particles in oil contributes to different dropicle configurations in subsequent experiments (Sections 2.2–2.4).

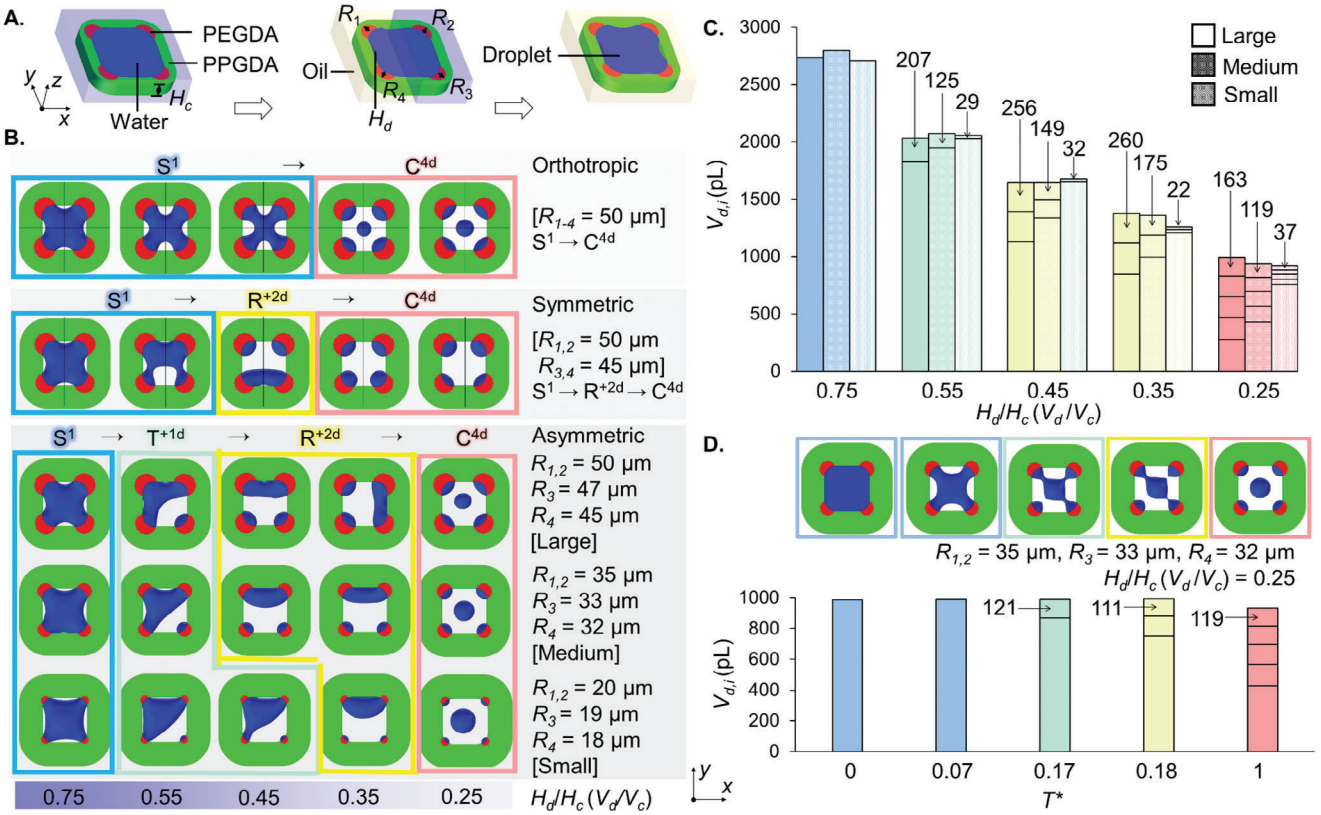


**Figure 3.** A) Schematic of the droplet formation within a 4C amphiphilic particle upon medium exchange from EtOH to PBS to Oil. B) Three numerical models, orthotropic, symmetric, and asymmetric, are solved to systematically obtain different droplet configurations for variable $H_d/H_c$ ratio. In the asymmetric model, the hydrophilic patch radii ($R_{1\text{-}4}$) are varied from large to medium to small combinations to realize the droplet transition from $S^1 \rightarrow T^{+1d} \rightarrow R^{+2d} \rightarrow C^{4d}$ for variable $H_d/H_c$ ratio. C) A quantitative analysis of the individual droplet volumes ($V_{d,i}$) for different droplet configurations and $H_d/H_c$ ratio. The stacked bars represent the volume of each droplet in configurations with multiple droplets per particle. D) A time-dependent simulation highlights the droplet transition over time as the total aqueous volume is split into smaller volumes $V_{d,i}$.

For particles $F_1$ to $F_{16}$, the cavity diameter in EtOH increased by ≈25% from $D_c \approx 177$ to $\approx 221$ µm (Figure 2E). For any given particle type, the $D_c$ decreased from EtOH to PBS and increased back in oil, following a trend similar to $D_p$. For example, the $F_1$ particle cavity shrunk by ≈21% from EtOH to PBS and increased by ≈46% from PBS to oil. With a gradual increase in the flow rate ratio, $Q_{1,2,4}$:$Q_3$, from 1:1 to 16:1, the hydrophilic proportion within a particle receded, which left space for the innermost inert stream $Q_4$ to expand the cavity diameter. The hydrophilic patch diameter in EtOH also decreased significantly from $D_{PEG} \approx 95$ to ≈47 µm (i.e., ≈51% reduction) as the flow rate ratio was increased from $F_1$ to $F_{16}$ (Figure 2F). Contrary to the particle and cavity diameters ($D_p$ and $D_c$), the hydrophilic patch ($D_{PEG}$) expanded from EtOH to PBS and shrank in oil. For example, in the $F_1$ particles with $D_{PEG} \approx 95$ µm in EtOH, the PBS was absorbed by the hydrophilic patch to swell it to $D_{PEG} \approx 118$ µm (i.e., ≈24% increase). The oil phase pushed the PBS to a minimal surface energy configuration, resulting in the contraction of the hydrophilic patch with $D_{PEG} \approx 97$ µm (i.e., ≈18% reduction). A variable hydrophilic patch size for particles $F_1$ to $F_{16}$ was the most critical feature of the particles for variable dropicle formations.

### 2.2. Numerical Modeling of Dropicle Formation

An aqueous droplet is captured within the cavity of the 4C particle as the media is exchanged from EtOH to PBS to oil (**Figure 3A**). We established a two-phase flow 3D CFD model, based on our earlier reported 2D model,[33] to systematically investigate the mechanism driving different dropicle configurations within the particle cavities (Figure 3B–D). The dropicle configuration was influenced by the hydrophilic patch radii $R_{1\text{-}4}$ and the ratio of the droplet initial height ($H_d$) with respect to the particle cavity height ($H_c$). We modeled dropicle formation using orthotropic, symmetric, and asymmetric particle geometries for a range of $H_d/H_c$ values and a fixed simulation time (Figure 3B). The $H_d/H_c$ ratio corresponds to the ratio of the droplet to the particle cavity volumes ($V_d/V_c$), which varied from 0.75 to 0.25, assuming the cavity was never filled to its maximum capacity due to cavity expansion from PBS to oil (see Figure 2D). Notably, a ≈50% increase in $D_c$ from PBS to oil will expand the cavity volume by >2x. Therefore, it is reasonable to assume that the final cavity volume $V_c$ will always be larger than the volume of the droplet $V_d$ it encompasses. Hence, we performed the numerical simulations for $H_d/H_c$ or $V_d/V_c$ ranging from 0.75 to 0.25 to mimic the dropicle formation

as the droplet volume decreased over time (Figure S2, Supporting Information).

The orthotropic particle, with four identical patches at the corners, formed an $S^1$ droplet for $H_d/H_c = 0.75$, which transitioned directly to $C^{4d}$ droplets adhering to the four hydrophilic patches of the particle for $H_d/H_c \leq 0.35$ (Figure 3B). An orthotropic model can not produce the $T^{+1d}$ or $R^{+2d}$ configurations. The symmetric particle, with two pairs of identical hydrophilic patches, resulted in a similar $S^1$ droplet for $H_d/H_c = 0.75$, which transitioned to $R^{+2d}$ and then $C^{4d}$ droplets as the $H_d/H_c$ decreased to 0.45 and 0.35, respectively. The symmetric model is unable to produce the $T^{+1d}$ configuration. However, an asymmetric particle, with three distinct hydrophilic patch radii, encompassed all the dropicle configurations transitioning as follows: $S^1 \rightarrow T^{+1d} \rightarrow R^{+2d} \rightarrow C^{4d}$, as $H_d/H_c$ decreased from 0.75 to 0.25. Notably, a difference of $\lesssim$10% between the hydrophilic patch radii $R_{1\text{-}4}$ was enough to induce asymmetric dropicle shapes, i.e., $T^{+1d}$ and $R^{+2d}$. It was essential to model the dropicle formation with an asymmetric particle design to capture all four types of dropicle configurations by considering a diameter difference of ≈5–10% for the four hydrophilic patches to break the particle symmetry.

We simulated dropicle formation using particles with large, medium, and small radii combinations [$R_{1,2}$, $R_3$, $R_4$] of [50, 47, 45 µm], [35, 33, 32 µm], and [20, 19, 18 µm], respectively, for variable $H_d/H_c$ or $V_d/V_c$ values (Figure 3B; Movie S1, Supporting Information). We selected different radii $R_{1\text{-}4}$ values within a single particle to model the slight variability between the hydrophilic patches due to uneven or decaying UV exposure within the microchannel during the particle fabrication. For all asymmetric particle models, we obtained a gradual transition of dropicle configurations from $S^1 \rightarrow T^{+1d} \rightarrow R^{+2d} \rightarrow C^{4d}$ as the $H_d/H_c$ decreased from 0.75 to 0.25. For the small radii combination, the dropicle transitioned from $T^{+1d} \rightarrow R^{+2d}$ as the $H_d/H_c$ decreased from 0.45 to 0.35, whereas the $R^{+2d}$ configuration could only be observed for a very narrow range of $H_d/H_c$ values. The large hydrophilic patches exert a relatively greater pull on the aqueous droplet toward the corners due to the wettability of the patches for a constant PBS-oil interfacial tension. Therefore, the dropicle transitioned early from $T^{+1d} \rightarrow R^{+2d}$ as the PBS volume fraction ($V_d/V_c$) decreased below 0.55 for large and medium patches. For the small patches, the wetting force pulling the droplet toward the corners was not strong enough; therefore, the $T^{+1d}$ configuration was retained for $0.55 \geq V_d/V_c \geq 0.45$. However, a further reduction in droplet volume resulted in a transition to $R^{+2d}$ dropicles for $V_d/V_c = 0.35$ and finally to $C^{4d}$ dropicles for $V_d/V_c = 0.25$. If we associate the large patch radii with higher droplet volume (i.e., $V_d/V_c = 0.75$) retained within the cavity, one can easily deduce that the most stable dropicle configuration will be $S^1$. On the contrary, the small patch radii with lower droplet volume (i.e., $V_d/V_c = 0.25$) retained within the cavity will consistently result in the $C^{4d}$ dropicles. The other configurations, i.e., $T^{+1d}$ and $R^{+2d}$, will fall in between the large and small patch radii. The discretely patterned hydrophilic patches enabled a droplet transition trend that was largely uninfluenced by the shape of the amphiphilic microparticles. The dropicle configurations were influenced by the ratio, $R_c/R_{PEG}$, of the radius of the inscribed circle passing through the patch centers ($R_c$) to the patch radius ($R_{PEG}$)(Figures S3 and S4, Supporting Information).

A quantitative analysis of dropicle formation revealed that the 4C particles with $D_c$ of 200 µm can form droplets with a wide range of volumes ranging from >2.5 nL to <100 pL (Figure 3C). The 4C particles, irrespective of hydrophilic patch size, formed single $S^1$ dropicles with volumes of ≈2.75 nL for $V_d/V_c$ of 0.75. For $V_d/V_c = 0.55$, the dropicles transitioned from $S^1$ to $T^{+1d}$ configuration. For the large patch particle, we obtained the $T^{+1d}$ configuration with two droplets of ≈207pL and ≈1.80 nL volume, respectively. The medium and small patch particles were able to form even smaller droplets of ≈125 and ≈29 pL, respectively, at one corner of the particle cavity with $T^{+1d}$ configuration, which can be attributed to the reduced patch sizes. For $V_d/V_c = 0.45$, the 4C particles with large and medium patches formed dropicles with $R^{+2d}$ configuration with the volume of the smallest droplets as ≈256 and ≈149 pL, respectively. The particles with small patches could still retain two $T^{+1d}$ dropicles with volumes of ≈1.65 nL and ≈32 pL. For $V_d/V_c = 0.35$, all the particles resulted in an $R^{+2d}$ configuration. Similarly, for $V_d/V_c = 0.25$, all the particles resulted in the $C^{4d}$ configuration with four droplets formed at the four corners of the cavity and a satellite droplet at the center. The average volumes of the four $C^{4d}$ droplets were ≈181, ≈127, and ≈41 pL for the large, medium, and small patch particles, respectively. These results indicated that we can obtain smaller droplets within the 4C amphiphilic particle by adjusting the patch size without changing the particle size. A small variation in total aqueous volume between simulations can arise from the numerical error. Moreover, a droplet diameter below a critical value can shrink due to the diffusion of the aqueous phase in the numerical models, leading to the variation in overall aqueous volume between the simulations.[34,35] The numerical total volume decreased by ≈2.5× from $S^1$ to $C^{4d}$ droplet for the large, medium, and small cases, respectively. Time-dependent numerical models enabled us to analyze the dropicle shape transition over a normalized time scale $T^*$ (Figure 3D). For medium-sized hydrophilic patches and $V_d/V_c$ of 0.25, the droplet shape transitioned from $S^1 \rightarrow T^{+1d} \rightarrow R^{+2d} \rightarrow C^{4d}$ at $T^* = 0.07$, 0.17, 0.18, and 1.00, respectively. The total aqueous volume within the cavity remained constant at ≈990 pL, which gradually split from a single droplet to four isolated droplets at the corners of the particle and one satellite droplet in the middle of the cavity with volumes as low as ≈119 pL.

### 2.3. Experimental Analysis of Dropicle Formation

We experimentally investigated the dropicle formation using different 4C particles ($F_1$-$F_{16}$) as the hydrophilic patches of variable sizes retained matching PBS volumes within the particle cavities, sealed by the immiscible oil phase (**Figure 4A**). The experimental results agreed well with the corresponding numerical models built using different $V_d/V_c$ ratios and hydrophilic patch radii combinations ($R_{1,2}$, $R_3$, $R_4$), i.e., large, medium, small, and small, which represented the $F_1$, $F_9$, $F_{12}$, and $F_{16}$ particles, respectively (Figure 4B). The average patch diameters of $95 \pm 5$, $71 \pm 4$, $52 \pm 4$, and $47 \pm 5$ µm measured experimentally for the $F_1$, $F_9$, $F_{12}$, and $F_{16}$ particles were similar to those in the numerical simulations 96 (large), 68 (medium), 39 (small), and 39 µm (small) (Table S1, Supporting Information). The $S^1$ dropicles within $F_1$ particles corresponded to the large hydrophilic patches that

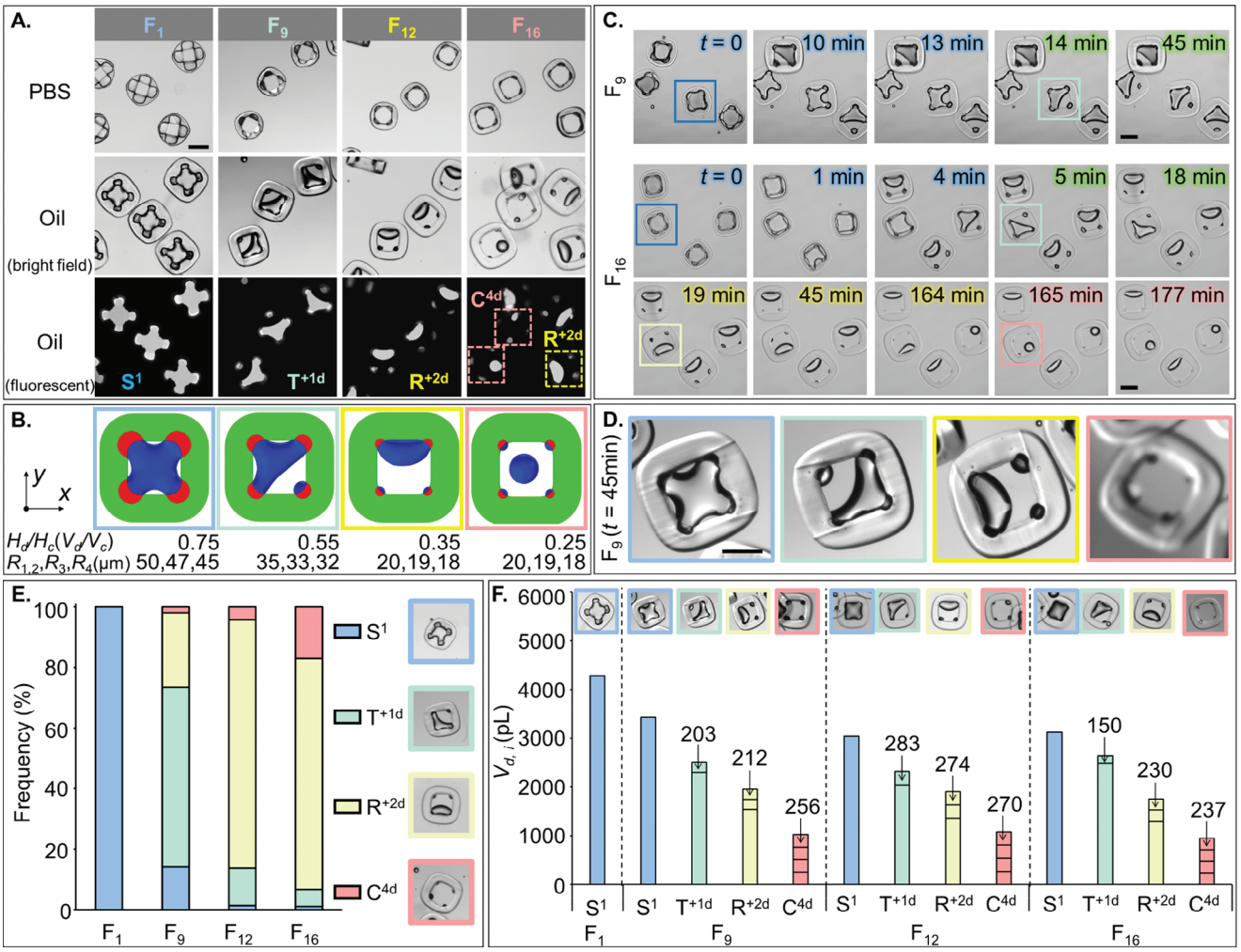


**Figure 4.** A) Experimental observation of the dropicle formation within $F_1$, $F_9$, $F_{12}$, and $F_{16}$ particles at $t$ = 45 min. Upon addition of the oil phase, aqueous PBS dropicles (visible in the bright field and fluorescent images) were captured within the particle cavities. B) Numerical models of the dropicle formation within particles with variable hydrophilic patch radii match well with the experimental results in (A). Panel (B) is adopted from Figure 3B. C) Transition of dropicle configurations over time within $F_9$ ($S^1 \rightarrow T^{+1d}$) and $F_{16}$ ($S^1 \rightarrow T^{+1d} \rightarrow R^{+2d} \rightarrow C^{4d}$) particles. D) A close-up view of a single $F_9$ particle with four dropicle configurations reached at $t$ = 45 min. E) Frequency distributions of $S^1$, $T^{+1d}$, $R^{+2d}$, and $C^{4d}$ dropicles within $F_1$, $F_9$, $F_{12}$, and $F_{16}$ particles. F) The average volume of individual droplets $V_{d,i}$ within the $S^1$, $T^{+1d}$, $R^{+2d}$, and $C^{4d}$ dropicles captured by the $F_1$, $F_9$, $F_{12}$, and $F_{16}$ particles. Scale bars: 200 μm.

captured the highest aqueous volume during the dropicle formation, which was numerically modeled with $V_d/V_c$ = 0.75 to result in the same $S^1$ dropicle configuration. As the hydrophilic patches decreased from a large size in $F_1$ particles to a medium size in $F_9$ particles, the capability of holding aqueous volume within the $F_9$ cavities significantly decreased. Therefore, the numerical model for the $F_9$ particle was established with $V_d/V_c$ = 0.55, resulting in the $T^{+1d}$ configuration. For the $F_{12}$ and $F_{16}$ particles with small hydrophilic patches, $V_d/V_c$ values of 0.35 and 0.25, respectively, were adopted in the numerical models, yielding the $R^{+2d}$ and $C^{4d}$ configurations. The experimental phenomena aligned well with the numerical results. We experimentally obtained two different $C^{4d}$ dropicles for the $F_9$, $F_{12}$, and $F_{16}$ particles individually, which resulted from the uneven distribution of the four droplets split from the $R^{+2d}$ shape (Figure S5, Supporting Information).

A dropicle formed within a given 4C particle can transition from one configuration to the next over time (Figure 4C; Movie S2 and Movie S3, Supporting Information). For example, $S^1$ dropicles formed inside the $F_9$ particles at $t$ = 0 min gradually transitioned to a stable $T^{+1d}$ configuration at $t$ = 45 min. We could observe a complete transition of dropicle configurations from $S^1 \rightarrow T^{+1d} \rightarrow R^{+2d} \rightarrow C^{4d}$ within $F_{16}$ particles observed for ≈3 h. The transition from $S^1 \rightarrow T^{+1d} \rightarrow R^{+2d}$ occurred within the first 19 min because the cavity gradually expanded in oil as the hydrophobic layer absorbed oil over time. The $R^{+2d}$ remained the most dominant and stable configuration from $t$ = 19 to 45 min as the particle dimensions were already stabilized (the second dominant $C^{4d}$ configuration was not visible in the frame of view). For $t \geq$ 164 min, we saw the $R^{+2d}$ dropicles also transitioned to the $C^{4d}$ configuration. We ascribed this transition $R^{+2d} \rightarrow C^{4d}$ to a gradual decrease in the dropicle volume, resulting from the diffusion

of the aqueous phase to the oil phase. We calculated the diffusion rate of ≈10 pL $min^{-1}$ as the ≈2745 pL volume $S^1$ dropicle at $t$ = 0 min transition to ≈925 pL volume $C^{4d}$ dropicle at $t$ = 177 min. A single particle type can exhibit more than one dropicle configurations based on particle-to-particle variability during fabrication and a slightly different aqueous volume captured within the particles during the dropicle formation. For example, at a given time $t$ = 45 min after dropicle formation, the $F_9$ particles depicted all four of the dropicle configurations, i.e., $S^1$, $T^{+1d}$, $R^{+2d}$, and $C^{4d}$, at variable frequencies; however, the $T^{+1d}$ configuration remained the dominant one (Figure 4D,E).

We quantitatively characterized different dropicle configurations, i.e., $S^1$, $T^{+1d}$, $R^{+2d}$, and $C^{4d}$, formed within the $F_1$, $F_9$, $F_{12}$, and $F_{16}$ particles by plotting their frequency distributions (Figure 4E). The $F_1$, $F_9$, $F_{12}$, and $F_{16}$ particles resulted in predominantly $S^1$ (100%), $T^{+1d}$ (59%), $R^{+2d}$ (82%), and $R^{+2d}$ (76%) dropicles, respectively. The proportion of $S^1$ dropicles dropped to 14% for $F_9$ particles and <2% for $F_{12}$ and $F_{16}$ particles. Similarly, the proportion of $T^{+1d}$ decreased from 59% ($F_9$) to 13% ($F_{12}$) and 6% ($F_{16}$). However, the $R^{+2d}$ dropicle frequency increased from 25% ($F_9$) to 82% ($F_{12}$) and 76% ($F_{16}$). The highest proportion of $C^{4d}$ dropicles (17%) was obtained within the $F_{16}$ particles, which was significantly higher than the $C^{4d}$ proportion in $F_9$ (2%) and $F_{12}$ (4%) particles. The four different dropicle configurations, i.e., $S^1$, $T^{+1d}$, $R^{+2d}$, and $R^{+2d}$+$C^{4d}$, within the $F_1$, $F_9$, $F_{12}$, and $F_{16}$ particles corresponded to the cavity diameter ($D_c$) to hydrophilic patch diameter ($D_{PEG}$) ratio of 2.11, 2.82, 3.84, and 4.26, respectively. The $F_{16}$ particles, with $D_c/D_{PEG} < 5$, have enabled a relatively high proportion (≈17%) of the $C^{4d}$ dropicles. Our numerical analysis predicted that a higher proportion of the $C^{4d}$ dropicles can be achieved for $D_c/D_{PEG} > 5$ (Figures S3 and S4, Supporting Information). Therefore, the promising way to further minimize the droplet volume would be 1) to reduce the hydrophilic patch size by adequately adjusting the flow rate ratio, or 2) to enlarge the cavity diameter by employing a larger capillary during the particle fabrication. The data for $F_2$ and $F_4$ dropicles are included in Figure S6 (Supporting Information).

Moreover, we plotted the average volume of individual droplets $V_{d,i}$ captured inside the 4C particles (Figure 4F). The average $S^1$ dropicle volume calculated for $F_1$ particles was ≈4.3 nL, which decreased to ≈3.4 nL for $F_9$ particles due to the shearing stress from a fluid flow during the solution exchange from PBS to oil. The larger hydrophilic patches enabled stronger wettability to counteract the shearing effect. The $F_9$ particles also formed $T^{+1d}$, $R^{+2d}$, and $C^{4d}$ dropicles, where the smallest average dropicle volume was recorded for $T^{+1d}$ configuration at ≈203 pL. The volumes of individual droplets within $S^1$, $T^{+1d}$, $R^{+2d}$, and $C^{4d}$ configurations decreased further for the $F_{12}$ particle, confirming that smaller hydrophilic patches retain lower droplet volume. The volumes of dominant $R^{+2d}$+$C^{4d}$ dropicles decreased from $F_{12}$ to $F_{16}$ particles, and we measured the smallest average volume of ≈150 pL for the $T^{+1d}$ dropicle captured within $F_{16}$ particles. See Figure S5 (Supporting Information) for the detailed average volume distributions of individual $S^1$, $T^{+1d}$, $R^{+2d}$, and $C^{4d}$ ($[C^{4d}]_I$ and $[C^{4d}]_{II}$) droplets. The experimental total volume reduced from ≈3200 to ≈1000 pL (≈3×) for $F_9$, $F_{12}$, and $F_{16}$ dropicles, showing agreement with the numerical data (Figures 3C and 4F).

### 2.4. Comparison Between Amphiphilic Particles with Continuous and Discrete Hydrophilic Layers

To analyze the influences of the continuous and discrete hydrophilic layers on the dropicle formation within an amphiphilic particle, we compared the particle dimensions and dropicle configurations between the O-shaped and 4C amphiphilic particles with $D_p$ = ≈400 µm (**Figure 5**). The experimental data for the O-shaped particle was adapted from our previous work.[3] We calculated the contraction (−) and expansion (+) rates (Δ) of the measured particle diameter $D_p$, cavity diameter $D_c$, hydrophilic layer thickness $T_{PEG}$ (*O*-shaped particle), and hydrophilic patch diameter $D_{PEG}$ (4C particle), for medium exchange from EtOH → PBS and from PBS → oil, respectively (Figure 5A). All the dimensions of the 4C particle changed less than that of the O-shaped particle during the media exchange. For EtOH → PBS exchange, the O-shaped particles shrank relatively more with −16% $\Delta D_p$ and −32% $\Delta D_c$, compared to the 4C particles, having inner discontinuous hydrophilic patches, with −11% $\Delta D_p$ and −21% $\Delta D_c$. For PBS → oil exchange, the $\Delta D_p$ and $\Delta D_c$ values for the 4C particle, i.e., +30% and +46%, were smaller than that of the O-shaped particle, i.e., +37% and +58%, respectively. For PBS → oil exchange, the $\Delta T_{PEG}$ of −30% for the O-shaped particle was higher than the $\Delta D_{PEG}$ of −18% for the 4C particle.

We further simulated the aqueous volume distributions within the O-shaped and 4C particles with varying $V_d/V_c$ values (Figure 5B). A droplet filled the cavity of the O-shaped particle entirely when $V_d/V_c$ = 0.75. However, the cylindrical droplet transitioned to a single annular ring-shaped droplet gradually at $V_d/V_c$ = 0.45. For $V_d/V_c$ = 0.25, two separated droplets were formed, adhering to the inner hydrophilic layer of the particle accompanied by a satellite droplet at the cavity center. Notably, the hydrophilic surface wettability dominated the force balance with the water-oil interfacial tension to result in a thinner ring-shaped droplet or two segregated droplets clinging to the inner layer of the particle. For a stable circular droplet obtained experimentally,[3] the O-shaped particles should capture a sufficient volume of water inside its cavity, which corresponds to $V_d/V_c$ = 0.75. Comparatively, the 4C dropicles resulted in very different configurations and multiple droplets driven by the discrete hydrophilic patches as described above. Lastly, we have plotted the total dropicle volume ($V_d$) to hydrophilic wetting surface area ($S_{PEG}$) ratio ($V_d/S_{PEG}$) for the 4C and O-shaped particles (Figure 5C). The $V_d/S_{PEG}$ ratio increased by ≈1.8×, ≈2.5×, and ≈4.4× for the 4C particles with large, medium, and small hydrophilic patches, respectively, when compared with the O-shaped particles. Such ability to vary the $V_d/S_{PEG}$ ratio can enable new bioassay development with tunable sensitivities and dynamic ranges.

## 3. Methods

### 3.1. Numerical Modeling

#### *3.1.1. Simulation for Particle Shape Prediction*

To predict the particle's shape and dimensions under different flow rate ratios, we adopted the "Two-Phase Flow, Level Set" module in COMOSL Multiphysics 6.1 to run laminar flow streams of

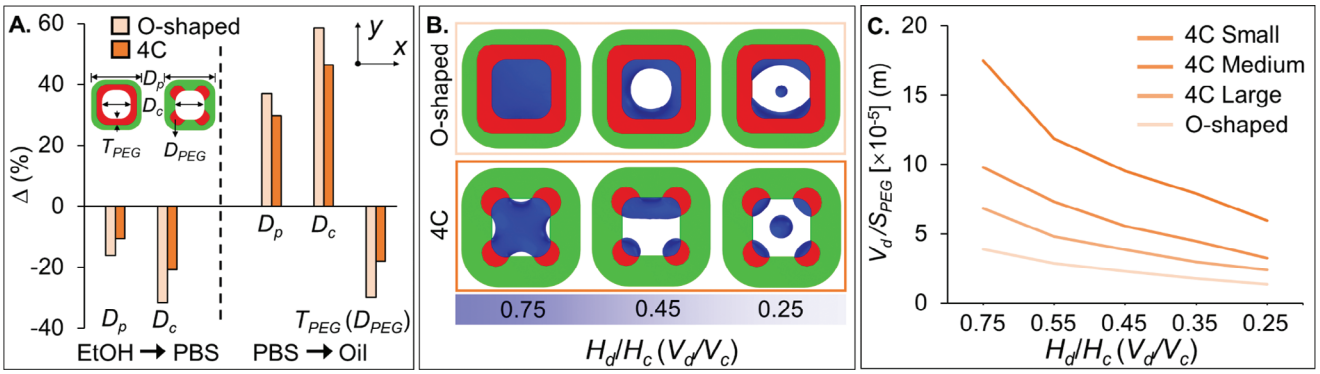


**Figure 5.** Comparison between the O-shaped and 4C particles. A) The contraction and expansion rates of the particle diameter $D_p$, cavity diameter $D_c$, thickness $T_{PEG}$ (O-shaped particle), and diameter $D_{PEG}$ (4C particle) of the hydrophilic layer in EtOH, PBS, and oil. B) Simulated dropicle formation within the O-shaped and 4C particles (large hydrophilic patches) with different $H_d/H_c$ values. Here, $D_p = 400$ µm, $D_c = 200$ µm, $T_{PEG} = 50$ µm, and $R_{1,2}$, $R_3$, $R_4 = 50, 47, 45$µm. C) Total droplet volume $V_d$ to hydrophilic surface area $S_{PEG}$ ratio for the O-shaped and 4C dropicles with different hydrophilic patch sizes.

variable velocities through an outlet microchannel with a dimension of 0.5 mm (Model S1, Supporting Information). To reduce the computing time, we established a quarter model of the microchannel (Figure 2A). The interfacial tension between the two streams was set as zero to emulate minimal free surface energy between the partially miscible streams. The viscosities of the inner hydrophilic and outer hydrophobic streams were set to be 0.007 and 0.042 Pa·s, respectively. The density of the two flow streams was constant, 987 kg $m^{-3}$. The contact angle of the interface with the wetted walls of the microchannel was 90°. The flow rate ratio between the four streams $Q_1$:$Q_2$:$Q_3$:$Q_4$ was altered to obtain particle shapes with variable thicknesses of the discrete hydrophilic patches and the continuous hydrophobic layer of the particle. The total flow rate for the four inlets was 2 mL $min^{-1}$. We also solved the "Laminar Flow" module to compare the results of the "Two-Phase Flow, Level Set" module with a single-phase flow model (Figure S1, Supporting Information).

### 3.1.2. Simulation for Dropicle Formation

We used the "Two-Phase Flow, Phase Field" module to simulate the various dropicle configurations formed inside the particle cavity (Model S2, Supporting Information). For optimal computing time, we established a vertically symmetric half model. An amphiphilic particle was modeled, containing a continuous outer hydrophobic layer and four hydrophilic patches at the corners of the particle. The cavity of the particle was uniformly filled with an aqueous solution at the onset of the simulation, whereas the oil phase surrounded the particle. The interfacial tension between the water and oil phases was 0.03 N $m^{-1}$. The contact angles that the interface would make with the hydrophilic and hydrophobic layers of the particle were fixed at 45° and 150°, respectively. The density and dynamic viscosity of the aqueous phase were 1000 kg $m^{-3}$ and 0.001 Pa·s, and that of the oil phase were 1050 kg $m^{-3}$ and 0.06 Pa·s, respectively. We employed an adaptive mesh, where a finer mesh region followed the water-oil interface as the simulation moved forward in time (Figure S7, Supporting Information). To trace the interface accurately, the water-oil interface thickness was set as 10× smaller than the default thickness value. The simulation output time was $T$ = 10 ms (Figures 3B,C and 4B). To evaluate the volume of individual droplets within a given 4C dropicle configuration, we partitioned the cavity domain into 16 smaller portions for the appropriate estimation of each droplet volume (Figure 3D,E). The simulation conditions for the O-shaped dropicle formation were identical to that of the 4C dropicle (Figure 5B).

## 3.2. Experimental

### 3.2.1. Particle Fabrication Using Stop-Flow Lithography

We introduced four polymer precursor streams mixed with a photoinitiator (Darocur 1173), i.e., inert hydrophobic polypropylene glycol (PPG), curable hydrophobic polypropylene glycol diacrylate (PPGDA), curable hydrophilic polyethylene glycol diacrylate (PEGDA), and inert hydrophilic polyethylene glycol (PEG), with different flow rates $Q_1$-$Q_4$ to the four inlets of the 3D printed microfluidic device (Model S3, Supporting Information) for sculpting the streams to enable a desired cross-sectional flow profile (Figure 1B; Figure S8, Supporting Information).[1–4] The inlets opened into four stacked microchannels separated by thin walls to prevent the premature mixing of streams (Figure 1B). Notably, inlet 3 was further divided into four separated yet identical subchannels to bring four uniform streams ($3_i$-$3_{iv}$) of the curable hydrophilic precursor to the device. The four main streams 1–4 flowed along their respective microchannels and sequentially merged at a tapered region of the device close to the outlet to enable a multi-layered structured co-flow of hydrophilic and hydrophobic precursors inside a square glass capillary. Four syringe pumps, a pinch valve, and UV light were controlled using a Labview script to perform the cyclic stop-flow lithography process for the 4C amphiphilic microparticle fabrication (Figure S8, Supporting Information). The flow stopped entirely within a short delay time ($t_d$) after the four syringes were turned off as the pinch valve closed simultaneously. When exposed to UV light for exposure time ($t_{exp}$), the curable precursor streams polymerized under a photomask to form amphiphilic microparticles with discontinuous inner hydrophilic patches and a continuous outer

hydrophobic layer. The cured particles were flushed for a flow stabilization time ($t_s$) and collected in the tube as the pinch valve was opened, and the syringe pumps were turned on to generate a stable co-flow within the outlet of the device. The rectangular slits in the photomask defined the particle height ($H_p$), whereas the flowrates $Q_1$-$Q_4$ influenced the particle ($D_p$), cavity ($D_c$), and hydrophilic patch ($D_{PEG}$) diameters. Compared to a concentric O-shaped amphiphilic particle with a continuous inner hydrophilic layer,[2,3,5] the 4C particle has four independent hydrophilic patches at the corners (Figure 1C). The particles were washed and collected in the EtOH solution for the subsequent dropicle formation.

#### 3.2.2. Dropicle Formation

The workflow to form the particle-templated droplets within the 4C amphiphilic particle was based on simple pipetting and washing steps (Figure 3A). First, the particles suspended in EtOH were transferred to a well plate, followed by a medium exchange to a PBS solution. The hydrophilic patches swelled after absorbing the aqueous PBS solution, whereas the outer hydrophobic layer contracted. Second, the excess PBS was removed, and the oil (poly(dimethylsiloxane-co-diphenylsiloxane), dihydroxy terminated, Sigma-Aldrich) was added to the well plate to push away the aqueous phase outside the particles due to the immiscibility between the water and oil phases. The continuous oil phase encapsulated the droplets inside each 4C amphiphilic particle.

#### 3.2.3. Dropicle Volume Calculation

The top cross-sectional areas of the dropicle were measured from the brightfield (Figure 4C) or fluorescent (Figure 4F) images using ImageJ software.[36] Simple multiplication of areas with the particle or cavity height ($H_c$) would lead to an overestimation of dropicle volume. Here, we take a ratio of the volumes of a sphere to a cylinder with the same cross-sectional area in the top view, *viz.*, $V_{sphere}$: $V_{cylinder}$, to obtain a correction factor of 0.67. We multiplied the factor 0.67 with the measured droplet area and $H_c$ to calculate the average volumes of the $S^1$, $T^{+1d}$, $R^{+2d}$, and $C^{4d}$ dropicles (Figure 4F; Figure S5, Supporting Information). To estimate the dropicle diffusion/evaporation rate, we measured the average droplet volumes at $t = 0$ min and $t = 177$ min from Movie S3 (Supporting Information), respectively. The dropicle volume at $t = 0$ min was obtained by multiplying the droplet area by $H_c$, without a correction factor, as the dropicle is assumed to completely fill the cavity. For computing the dropicle volume at $t = 177$ min, we multiplied the droplet area by $H_c$ and 0.67.

### 3.3. Statistical Analysis

We have presented the data as mean ± standard deviation (SD), wherever possible.

## 4. Conclusion

We have proposed 4C amphiphilic particles composed of an outer continuous hydrophobic layer embedded with four inner discrete hydrophilic patches at the corners, where the patch size could be readily tuned by modulating the flow rate ratio during particle fabrication. The 4C particles fabricated with different hydrophilic patch sizes can retain dropicles in four different configurations. We have conducted systematic numerical simulations for particle shape prediction and dropicle formation within the particle cavity. We have experimentally measured and characterized the particle dimensions in EtOH, PBS, and oil, showing good agreement with the simulation results. The numerical simulations informed that the dropicle formation was influenced by the hydrophilic patches and water volume captured inside the cavity of the particle. We have observed the dimension- and time-dependent transition trend, i.e., $S^1 \rightarrow T^{+1d} \rightarrow R^{+2d} \rightarrow C^{4d}$, for the dropicle formation within the 4C particles. The $F_{16}$ particles have enabled a relatively high proportion (≈17%) of the $C^{4d}$ dropicles of ≈200 pL volume, with an average hydrophilic patch diameter of ≈50 µm within a ≈200 µm cavity. This indicated that we can reduce the hydrophilic patch size or enlarge the particle cavity to further minimize the droplet volume. The 4C particles captured a wide range of dropicle volumes (≈200 pL to ≈4 nL), where a single 4C particle could hold up to four droplets within its cavity. Moreover, we have compared the dropicle formation within the 4C and O-shaped particles and deduced that the 4C particles could offer a much higher dropicle volume to wetting surface area ratio. Our work can inform the design of droplet volume and number per particle for developing new amplification bioassays with smaller droplets. The 4C particles with tunable dropicle configurations can lay a foundation for multiplexed high-sensitivity diagnostic assays.

## Supporting Information

Supporting Information is available from the Wiley Online Library or from the author.

## Acknowledgements

X.S. and S.U. contributed equally to this work. X.S. gratefully acknowledges the Sino-German (CSC-DAAD) Postdoc Scholarship Program, 2022 (57607866). This work was supported by the German Research Foundation (DFG) project numbers 538269976 and 539433772.

Open access funding enabled and organized by Projekt DEAL.

## Conflict of Interest

The authors declare no conflict of interest.

## Data Availability Statement

The data that support the findings of this study are available in the supplementary material of this article.

## Keywords

3D printing, additive manufacturing, computational fluid dynamics, droplets, lab on a particle, microfluidics, numerical simulation, particle-templated droplet

Received: September 9, 2024
Revised: November 25, 2024
Published online: December 24, 2024

[1] C. Y. Wu, M. Ouyang, B. Wang, J. D. Rutte, A. Joo, M. Jacobs, K. Ha, A. L. Bertozzi, D. Di Carlo, *Sci. Adv.* **2020**, *6*, eabb9023.
[2] G. Destgeer, M. Ouyang, C. Y. Wu, D. Di Carlo, *Lab Chip* **2020**, *20*, 3503.
[3] G. Destgeer, M. Ouyang, D. Di Carlo, *Anal. Chem.* **2021**, *93*, 2317.
[4] V. Shah, X. Yang, A. Arnheim, S. Udani, D. Tseng, Y. Luo, M. Ouyang, G. Destgeer, O. B. Garner, H. C. Koydemir, A. Ozcan, D. Di Carlo, *ACS Nano* **2023**, *17*, 19952.
[5] M. U. Akhtar, M. A. Sahin, H. Werner, G. Destgeer, *Adv. Mater. Technol.* **2024**, *9*, 2301967.
[6] Y. Yang, S. Vagin, B. Rieger, G. Destgeer, *Macro. Rap. Comm.* **2024**, *45*, 2300721.
[7] Q. Liu, M. Zhao, S. Mytnyk, B. Klemm, K. Zhang, Y. Wang, D. Yan, E. Mendes, J. H. V. Esch, *Angew. Chem.* **2019**, *131*, 557.
[8] H. Miwa, R. Dimatteo, J. de Rutte, R. Ghosh, D. Di Carlo, *Microsyst. Nanoeng.* **2022**, *8*, 84.
[9] T. W. Song, S. D. Kim, D. Y. Oh, Y. Lee, A. C. Lee, Y. Jeong, H. J. Bae, D. Lee, S. Lee, J. Kim, S. Kwon, *Adv. Sci.* **2019**, *6*, 1801380.
[10] C. Liu, X. Xu, B. Li, B. Situ, W. Pan, Y. Hu, T. An, S. Yao, L. Zheng, *Nano Lett.* **2018**, *18*, 4226.
[11] M. Y. H. Tanga, H. C. Shum, *Lab Chip* **2016**, *16*, 4359.
[12] K. Jin, C. Hu, S. Hu, C. Hu, J. Li, H. Ma, *Lab Chip* **2021**, *21*, 2892.
[13] Y. Wang, V. Shah, A. Lu, E. Pachler, B. Cheng, D. Di Carlo, *Lab Chip* **2021**, *21*, 3438.
[14] D. J. Collins, A. Neild, A. deMello, A. Liu, Y. Ai, *Lab Chip* **2015**,*15*, 3439.
[15] L. Mazutis, J. Gilbert, W. L. Ung, D. A. Weitz, A. D. Griffiths, J. A. Heyman, *Nat. Protoc.* **2013**, *8*, 870.
[16] H. N. Joensson, H. A. Svahn, *Angew. Chem., Int. Ed.* **2012**, *51*, 12176.
[17] J. de Rutte, R. Dimatteo, M. M. Archang, M. v. Zee, D. Koo, S. Lee, A. C. Sharrow, P. J. Krohl, M. Mellody, S. Zhu, J. V. Eichenbaum, M. Kizerwetter, S. Udani, K. Ha, R. C. Willson, A. L. Bertozzi, J. B. Spangler, R. Damioseaux, D. Di Carlo, *ACS Nano* **2022**, *16*, 7242.
[18] M. N. Hatori, S. C. Kim, A. R. Abate, *Anal. Chem.* **2018**, *90*, 9813.
[19] Y. Minagawa, H. Ueno, K. V. Tabata, H. Noji, *Lab Chip* **2019**, *19*, 2678.
[20] Q. Zhu, L. Qiu, B. Yu, Y. Xu, Y. Gao, T. Pan, Q. Tian, Q. Song, W. Jin, Q. Jin, Y. Mu, *Lab Chip* **2014**, *14*, 1176.
[21] D. Witters, B. Sun, S. Begolo, J. Rodriguez-Manzano, W. Robles, R. F. Ismagilov, *Lab Chip* **2014**, *14*, 3225.
[22] V. Yelleswarapu, J. R. Buser, M. Haber, J. Baron, E. Inapuri, D. Issadore, *Proc. Natl. Acad. Sci. USA* **2019**, *116*, 4489.
[23] M. T. Guo, A. Rotem, J. A. Heyman, D. A. Weitz, *Lab Chip* **2012**, *12*, 2146.
[24] M. A. Sahin, M. Shehzad, G. Destgeer, *Small* **2024**, *20*, 2307956.
[25] D. Dendukuri, S. S. Gu, D. C. Pregibon, T. Alan Hatton, P. S. Doyle, *Lab Chip* **2007**, *7*, 818.
[26] S. C. Chapin, P. S. Doyle, *Anal. Chem.* **2011**, *83*, 193.
[27] K. S. Paulsen, Y. Deng, A. J. Chung, *Adv. Sci.* **2018**, *5*, 1800252.
[28] D. Dendukuri, S. S. Gu, D. C. Pregibon, T. A. Hatton, P. S. Doyle, *Lab Chip* **2007**, *7*, 818.
[29] H. Lee, J. Kim, H. Kim, J. Kim, S. Kwon, *Nat. Mater.* **2010**, *9*, 745.
[30] S. E. Chung, W. Park, S. Shin, S. A. Lee, S. Kwon, *Nat. Mater.* **2008**, *7*, 581.
[31] K. Ha, J. D. Rutte, D. Di Carlo, A. L. Bertozzi, *J. Eng. Math.* **2022**, *134*, 1.
[32] R. S. Du, L. Liu, S. Ng, S. Sambandam, B. H. Adame, H. Perez, K. Ha, C. Falcon, J. D. Rutte, D. Di Carlo, A. L. Bertozzi, *Phys. Rev. E* **2021**, *104*, 015109.
[33] X. Song, G. Destgeer, *Phys. Fluids* **2024**, *36*, 012101.
[34] C. Zhang, Z. Guo, *Phys. Rev. E* **2019**, *100*, 061302(R).
[35] P. Yue, C. Zhou, J. J. Feng, *J. Comput. Phys.* **2007**, *223*, 1.
[36] C. A. Schneider, W. S. Rasband, K. W. Eliceiri, *Nat. Methods* **2012**, *9*, 671.